COMMUNICATION

Check for updates

Combining dithieno[3,2-*f*:2′,3′-*h*]quinoxaline-based terpolymer and ternary strategies enabling high-efficiency organic solar cells†

Sungwoo Jung,[a] Seonghun Jeong,[a] Jiyeon Oh,[a] Seoyoung Kim,[a] Seunglok Lee,[a] Seong-Jun Yoon [ORCID] *[a] and Changduk Yang [ORCID] *[ab]

By incorporating a dithieno[3,2-*f*:2′,3′-*h*]quinoxaline unit into a PM6 polymer backbone, we developed a novel terpolymer family, demonstrating composition-dependent optical, electrochemical, and morphological characteristics. Organic solar cells based on the combination of a terpolymer and ternary strategy achieved a high power conversion efficiency of 17.60%, demonstrating the validity of our combination strategy.

Recent progress in high-performance organic solar cells (OSCs) primarily relies on the combination of a wide-bandgap polymer donor and nonfullerene acceptor (NFA).[1–3] Substantial research has been focused on designing and synthesizing novel wide-bandgap polymer donors and NFAs. In the case of the NFAs, A–DA′D–A-type‡ molecular frameworks are one of the most popular design strategies following the development of the Y6 acceptor.[4–6] For polymer donors, D–A-type copolymer designs using weak electron donor and strong/medium electron acceptor units have been adopted for high-performing wide-bandgap polymers, resulting in the appearance of representative wide-bandgap donors PM6 and D18.[7–9] For the design and combination of wide-bandgap polymer donors and NFAs, the following attributes should be considered: (i) absorption complementarity, (ii) energy level matching, (iii) suitable phase separation, and (iv) molecular orientation/crystallinity tendency between the wide-bandgap polymer donor and NFA.[10–12] After finishing the new donor/acceptor synthesis stages, we sometimes encounter a mismatch with respect to these requirements. Therefore, instead of new skeleton design, donor/acceptor material development that preserves the primary π-conjugated backbone with a small

but significant variation is an efficient and cost-effective strategy for high-performance OSCs. For instance, side-chain engineering is one of the most effective development approaches for fine-tuning NFAs.[13–15] Terpolymerization is a promising method for developing high-performing wide-bandgap polymer donors.[16–19] In addition, ternary OSCs are another straightforward and dependable technique for high performance in terms of the supplementation of OSC devices.[20–22]

Recently, a dithieno[3,2-*f*:2′,3′-*h*]quinoxaline unit (referred to as Qx here; see Fig. 1a) has been reported as a new medium A unit for high-performance wide-bandgap polymer donors.[23] Inspired by the terpolymerization strategy, we introduce the Qx unit as the third unit into a representative high-performing wide-bandgap polymer donor PM6. Consequently, the OSCs based on the terpolymer PM6-Qx10 blended with N3 NFA exhibit higher photovoltaic performances than those based on PM6:N3. Furthermore, it was used as the third component on another representative high-performing wide-bandgap polymer D18-based ternary OSC, producing a further improved power conversion efficiency (PCE) of 17.60% while working in an alloy-like model.

The alternating copolymer (denoted as PM6) and random terpolymers (denoted as PM6-Qx10, PM6-Qx20, and PM6-Qx50) were synthesized using Stille coupling polymerization with the Qx proportion of 0%, 10%, 20%, and 50%, respectively (Fig. 1a). The proton nuclear magnetic resonance spectra were measured for all synthesized terpolymers (Fig. S1–S3, ESI†). The number-average molecular weights (M_n) and polydispersity index (PDI) of the four polymers were evaluated *via* high-temperature gel permeation chromatography (HT-GPC) at 100 °C using 1,2,4-trichlorobenzene as an eluent. The M_n values of PM6, PM6-Qx10, PM6-Qx20, and PM6-Qx50 were measured to be 38.1, 39.2, 39.3, and 39.6 kDa, with the corresponding polydispersity index (PDI) of 3.22, 2.98, 2.81, and 2.44, respectively (Fig. S4 and Table S1, ESI†). The similar M_n of the four polymers allowed us to ignore M_n-based factors. The thermal stability of the four polymers was assessed using thermogravimetric

[a] School of Energy and Chemical Engineering, Perovtronics Research Center, Low Dimensional Carbon Materials Center, Ulsan National Institute of Science and Technology (UNIST), 50 UNIST-gil, Ulju-gun, Ulsan 44919, South Korea. E-mail: yoonsj@unist.ac.kr, yang@unist.ac.kr

[b] Graduate School of Carbon Neutrality, Ulsan National Institute of Science and Technology (UNIST), 50 UNIST-gil, Ulju-gun, Ulsan 44919, South Korea
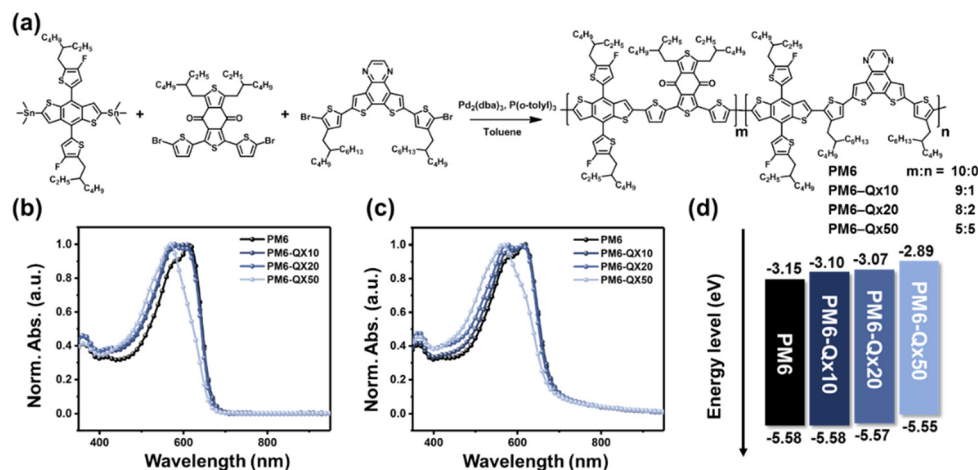
Fig. 1 (a) Synthetic routes and chemical structures of the alternating copolymer and random terpolymers. UV-Vis absorption spectra of the corresponding polymers in (b) dilute solution and (c) thin films. (d) Energy level diagrams of the corresponding polymers.

analysis. As shown in Fig. S5 (ESI†), the four polymers show similar thermal stability with 5% weight loss at the temperature of 420 °C, 421 °C, 425 °C, and 422 °C, respectively.

Fig. 1b and c display the ultraviolet-visible (UV-vis) absorption spectra of the four polymers in dilute chloroform solutions and thin films, respectively, and Table S1 (ESI†) provides pertinent data. In both film and solution states, these polymers exhibit two distinct absorption bands at 300–400 (π–π^* transition) and 500–660 nm (intramolecular charge transfer (ICT)), respectively, with a gradually blue-shifted absorption trend, as the proportion of Qx in the terpolymers rises. Notably, the PM6-Qx terpolymers show a stronger 0–1 vibrational transition peak relative to 0–0 with increasing Qx units, which can be attributed to the weaker ICT and aggregation behavior.

The electrochemical properties of the resultant polymers were investigated by cyclic voltammetry (CV) measurements (Fig. S6, ESI†), and CV-derived highest occupied molecular orbital (HOMO) and lowest unoccupied molecular orbital (LUMO) energy levels of the terpolymers are summarized in Table S1 (ESI†). It is noted that, as the portion of Qx increases, the HOMO energy levels of the terpolymers gradually rise in comparison with PM6, whereas the LUMO energy levels upshift considerably (Fig. 1d). Because there is no considerable difference in the HOMO energy levels, PM6- and PM6-Qx-based polymers can be used as donor materials, which works well with a representative NFA N3 (see Fig. S7 for the chemical structure of N3, ESI†).

To investigate the photovoltaic properties of the terpolymers, OSCs were fabricated using a conventional structure of indium–tin–oxide (ITO)/poly(3,4-ethylenedioxythiophene): poly(styrenesulfonate) (PEDOT:PSS)/active layer/perylenediimide functionalized with amino N-oxide (PDINO)/Al configuration, where the active layer consists of the terpolymer donor and the N3 acceptor. The fabrication details and procedures are described in the ESI.† The current density–voltage (J–V) curves of the optimized devices are displayed in Fig. 2a, and the relevant photovoltaic parameters are summarized in Table 1 and Table S2–S4 (ESI†). The optimized OSC based on PM6:N3 yields a PCE of 15.57%, with an open-circuit voltage (V_{OC}) of
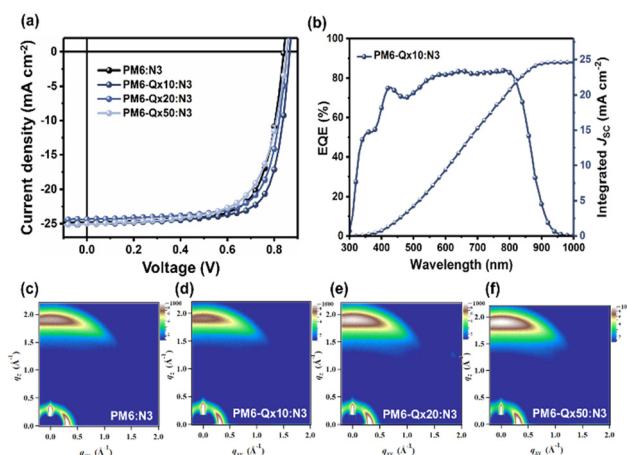

Fig. 2 (a) J–V curves of the fabricated OSCs based on the polymer donor:N3 blends. (b) Corresponding EQE spectra of the optimized device based on PM6-Qx10:N3. (c–f) 2D GIWAX images of PM6- and PM6-Qx-based blend films.

0.851 V, a short-circuit current density (J_{SC}) of 25.12 mA cm^{-2}, and a fill factor (FF) of 72.84%, which are similar to earlier reported results. Notably, despite the slightly upshifted HOMO

Table 1 Device parameters of OSCs based on the polymer donor:N3 and D18:PM6-Qx10:N3 under the illumination of AM 1.5G (100 mW cm^{-2})

Binary OSCs	V_{oc}[a] [V]	J_{sc}[a] [mA cm^{-2}]	FF[a] [%]	PCE[a] [%]
PM6:N3	0.851	25.12	72.84	15.57
PM6-Qx10:N3	0.863	25.43	74.80	16.43
PM6-Qx20:N3	0.852	24.76	73.29	15.46
PM6-Qx50:N3	0.851	25.00	68.56	14.58
Ternary OSCs (D18:PM6-Qx10:N3)				
1:0:1.6	0.841	26.18	78.02	17.16
0.9:0.1:1.6	0.843	26.27	78.13	17.31
0.8:0.2:1.6	0.848	26.50	78.34	17.60
0.7:0.3:1.6	0.851	25.89	77.42	17.05

[a] The statistical values are obtained from 16 cells.

levels upon adding Qx units, the PM6-Qx-based OSCs exhibited higher or comparable V_{OC} values than the PM6-based ones. It can be extrapolated that the improvement of the V_{OC} values is influenced by other parameters, including film morphology, charge recombination, and donor/acceptor interface, rather than the HOMO of the copolymer donor.[24] Among the optimized OSCs based on the PM6-Qx terpolymers, the PM6-Qx10-based one produced the best PCE of 16.43% with notable improvements in the V_{OC} of 0.863 V, J_{SC} of 25.43 mA cm^{-2}, and FF of 74.80%. These results show that the optimal amount of Qx unit addition in the PM6 backbone can improve the performance of the OSC devices. Fig. 2b displays the external quantum efficiency (EQE) spectra of the optimized devices, which span the spectrum range of 300–900 nm. The integrated J_{SC}s derived from the EQE spectra are in good agreement with those from the J–V characteristics within a 5% inaccuracy. The best-performing PM6-Qx10-based OSC has the highest overall EQE value.

J–V curves in the space-charge-limited current region are given in Fig. S8, ESI,† and the hole (μ_h) and electron (μ_e) mobility values were obtained and summarized in Table S5 (see the ESI† for the detailed device fabrication).[25] The devices based on the PM6-Qx10:N3 displayed the highest charge carrier mobility ($\mu_h = 5.81 \times 10^{-4}$ cm^2 V^{-1} s^{-1} and $\mu_e = 5.11 \times 10^{-4}$ cm^2 V^{-1} s^{-1}) and most balanced charge carrier transfer ($\mu_h/\mu_e = 1.14$), indicating better charge transport properties than other devices. These results reflect the high J_{SC} and FF observed for the PM6-Qx10:N3 system. Also, the light intensity (I)-dependent J–V characteristics were next investigated to learn more about the charge recombination of the devices, as illustrated in Fig. S9a and S9b (ESI†). A power-law equation $J_{SC} \propto I^\alpha$ expresses the relationship between J_{SC} and I, where α is the exponential factor related to the bimolecular recombination.[26] Additionally, the slope of nkT/q in the function $V_{OC} \propto nkT/q \ln(I)$ (k, T, and q stand for the Boltzmann constant, temperature (K), and elementary charge, respectively) indicates monomolecular recombination.[27] The PM6-Qx10:N3-based devices showed a higher $\alpha = 0.987$ and a lower slope of $1.36kT/q$ compared to other devices, indicating significantly less charge recombination characteristics. The above results show superior charge transport and reduced recombination features in the PM6-Qx10-based device, accounting for its higher photovoltaic performance.

To comprehend the impact of Qx units on the morphology/crystallinity/molecular packing of the terpolymer-based neat and blend films, atomic force microscopy and grazing-incidence wide-angle X-ray scattering (GIWAXS) studies were carried out. According to Fig. S10 (ESI†), compared with the PM6-based neat film (0.951 nm), all terpolymer-based ones exhibited smaller root mean square (RMS) roughness values ranging from 0.638 to 0.873 nm, indicating the weaker aggregation tendency of the PM6-Qx terpolymers. All the blend films exhibit uniformly distributed donor/acceptor phases together with lower RMS values, which is attributed to the good miscibility between the donor terpolymers and acceptor N3 (Fig. S11, ESI†). Additionally, with the rise in Qx proportion, the RMS values go from 0.475 to 0.545 nm, but these values remain lower than those of the PM6:N3 blend film (0.613 nm). The smooth and uniform surface of

the PM6-Qx10:N3 blend film has the lowest RMS value, which is advantageous for better contact with the transporting layers and electrodes. All neat films' GIWAXS data revealed identical microstructures with an in-plane (IP) (100) lamellar peak and an out-of-plane (OOP) (010) π–π stacking peak (Fig. S12a–d and S13a, ESI†), and pertinent parameters are listed in Table S6 (ESI†).

Interestingly, as the Qx portion rose, the PM6-Qx-based neat films showed more preferential face-on orientation in the vertical direction of the substrate. All the blend films have a predominant face-on orientation, as indicated by the strong OOP (010) π–π stacking peak (Fig. 2c–f and Fig. S13b, Table S7, ESI†). The trends of d-spacing and crystallite coherence lengths (CCLs) of the blend films in OOP are comparable to those of neat films. Notably, the PM6-Qx10-based blend films exhibited enhanced crystalline features, including decreased d-spacing$_{(010)}$ and increased CCL$_{(010)}$, contributing to effective charge transport in the vertical direction. Collectively, the optimal amount of Qx units in PM6 can positively affect the film morphology, molecular packing, and ordering characteristics.

To demonstrate the potential of PM6-Qx10 in OSCs, we developed ternary OSC devices based on the D18:N3 host platform (the chemical structure of D18 is shown in Fig. S14, ESI†). As the third component, the donor PM6-Qx10 possesses various benefits: (i) complementary absorption for those of the host platform, (ii) high compatibility due to the similar chemical structures of PM6-Qx10 and D18, and (iii) fine-tuning of the electrical and morphological features. The normalized absorption spectrum of PM6-Qx10 showed a positive complementarity to D18 and N3, as illustrated in Fig. S15 (ESI†). Contact angle measurements of all components in the ternary blend films were performed using deionized water and ethylene glycol to assess the compatibility of PM6-Qx10 and D18, as shown in Fig. S16, and relevant results are summarized in Table S8 (ESI†). Fig. 3a shows the surface energy and interfacial energy values for each neat film calculated according to the Owens–Wendt and Wu equations, respectively, yielding 21.19 mN m^{-1} (D18), 22.79 mN m^{-1} (PM6-Qx10), and 25.69 mN m^{-1} (N3), as well as 1.3855 mN m^{-1} (D18:N3), 1.6146 mN m^{-1} (PM6-Qx10:N3), and 0.0978 mN m^{-1} (D18: PM6-Qx10), respectively. The lowest value of interfacial energy implies good compatibility between PM6-Qx10 and D18, which benefits in forming the alloy-like phase.[28] We investigated the PM6-Qx10:D18 alloy further using CV measurements based on the PM6-Qx10 concentration (Fig. S17a, ESI†). Fig. S17b (ESI†) summarizes the trend of the HOMO energy
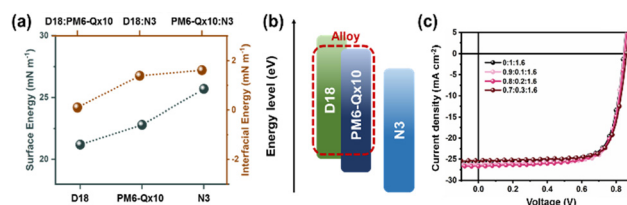

Fig. 3 (a) The trend of the calculated surface energy and interfacial energy of neat D18, PM6-Qx10, and N3 films. (b) Energy diagram of the D18:PM6-Qx10:N3 ternary system with alloying donor. (c) J–V curves of the fabricated ternary OSCs.

levels of the PM6-Qx10:D18 blends (ratios of 1:9, 2:8, and 3:7). Notably, when the PM6-Qx10 content rises, the HOMO energy level of the PM6-Qx10:D18 blends steadily drops, which is regarded as a typical alloy phase formation characteristic (the schematic illustration of the energy level in the alloy formation is depicted in Fig. 3b). PM6-Qx10:D18 alloy phase formation allows the donor to have finely adjusted energy levels without generating additional charge trap states, enabling high-performance ternary OSCs. Finally, we investigated the effect of PM6-Qx10, the third component, on photovoltaic performance. The host devices based on D18:N3 were fabricated according to the previously reported optimized process. Only the proportions of the two polymer donors (PM6-Qx10:D18 = 1:9, 2:8, and 3:7 (w/w)) were changed to evaluate the ternary devices. The J–V curves of the optimized devices are displayed in Fig. 3c, and relevant parameters are listed in Table 1. As expected, the V_{OC} values gradually increased as more PM6-Qx10 was added to the active layer. Notably, the optimal ternary devices with a 2:8 ratio of the two polymer donors exhibited a PCE of 17.60% with V_{OC}, J_{SC}, and FF values of 0.848 V, 26.50 mA cm^{-2}, and 78.34%, respectively. The corresponding results show the potential of PM6-Qx terpolymers as donors for high-performance OSCs.

In summary, we developed a novel terpolymer family by introducing Qx into a PM6 polymer backbone. The optical, electrochemical, morphological, and structural features, as well as the OSC performances, exhibited Qx-proportion-dependent tendencies in the resultant terpolymers. In particular, PM6-Qx10:N3 exhibited superior and well-balanced charge carrier transport properties with smooth and uniform surface morphologies, contributing to a higher PCE of 16.43% than that of PM6:N3 of 15.57%. By the surface/interfacial energy analyses and CV measurements, we revealed that the PM6-Qx10:D18 blend could successfully form an alloy phase. Ternary OSCs based on the D18:N3 host and PM6-Qx10 third component achieved a higher PCE of 17.60% than that of binary OSCs of 17.16%. This work demonstrates the high-efficiency OSCs by combining terpolymer and ternary strategies.

Conflicts of interest

There are no conflicts to declare.

Notes and references

‡ A: electron-withdrawing, D: electron-donating.

1 H. Bin, T. P. A. van der Pol, J. Li, B. T. van Gorkom, M. M. Wienk and R. A. J. Janssen, *Chem. Eng. J.*, 2022, **435**, 134878.
2 S. Holliday, R. S. Ashraf, A. Wadsworth, D. Baran, S. A. Yousaf, C. B. Nielsen, C.-H. Tan, S. D. Dimitrov, Z. Shang, N. Gasparini, M. Alamoudi, F. Laquai, C. J. Brabec, A. Salleo, J. R. Durrant and I. McCulloch, *Nat. Commun.*, 2016, **7**, 11585.
3 Y. Zhang, Y. Wang, R. Ma, Z. Luo, T. Liu, S.-H. Kang, H. Yan, Z. Yuan, C. Yang and Y. Chen, *Chin. J. Polym. Sci.*, 2020, **38**, 797–805.
4 J. A. Hong, M. Jeong, S. Park, A.-Y. Lee, H. S. Kim, S. Jeong, D. W. Kim, S. Cho, C. Yang and M. H. Song, *Adv. Sci.*, 2022, 2205127, DOI: 10.1002/advs.202205127.
5 S. Lee, G. Park, M. Jeong, B. Lee, S. Jeong, J. Park, Y. Cho, S. M. Noh and C. Yang, *ACS Appl. Mater. Interfaces*, 2022, **14**, 33614–33625.
6 H. Chen, R. Zhang, X. Chen, G. Zeng, L. Kobera, S. Abbrent, B. Zhang, W. Chen, G. Xu, J. Oh, S.-H. Kang, S. Chen, C. Yang, J. Brus, J. Hou, F. Gao, Y. Li and Y. Li, *Nat. Energy*, 2021, **6**, 1045–1053.
7 Q. Liu, Y. Jiang, K. Jin, J. Qin, J. Xu, W. Li, J. Xiong, J. Liu, Z. Xiao, K. Sun, S. Yang, X. Zhang and L. Ding, *Sci. Bull.*, 2020, **65**, 272–275.
8 M. Zhang, X. Guo, W. Ma, H. Ade and J. Hou, *Adv. Mater.*, 2015, **27**, 4655–4660.
9 J. Qin, L. Zhang, C. Zuo, Z. Xiao, Y. Yuan, S. Yang, F. Hao, M. Cheng, K. Sun, Q. Bao, Z. Bin, Z. Jin and L. Ding, *J. Semicond.*, 2021, **42**, 010501.
10 X. Xu, G. Zhang, Y. Li and Q. Peng, *Chin. Chem. Lett.*, 2019, **30**, 809–825.
11 A. Armin, W. Li, O. J. Sandberg, Z. Xiao, L. Ding, J. Nelson, D. Neher, K. Vandewal, S. Shoaee, T. Wang, H. Ade, T. Heumüller, C. Brabec and P. Meredith, *Adv. Energy Mater.*, 2021, **11**, 2003570.
12 J. Tang, C. Liao, Y. Duan, X. Xu, X. Deng, M. Yu, L. Li, R. Li and Q. Peng, *Angew. Chem., Int. Ed.*, 2022, **61**, e202213252.
13 F. Qi, L. O. Jones, K. Jiang, S.-H. Jang, W. Kaminsky, J. Oh, H. Zhang, Z. Cai, C. Yang, K. L. Kohlstedt, G. C. Schatz, F. R. Lin, T. J. Marks and A. K. Y. Jen, *Mater. Horiz.*, 2022, **9**, 403–410.
14 J. Lee, E. M. Go, S. Dharmapurikar, J. Xu, S. M. Lee, M. Jeong, K. C. Lee, J. Oh, Y. Cho, C. Zhang, M. Xiao, S. K. Kwak and C. Yang, *J. Mater. Chem. A*, 2019, **7**, 18468–18479.
15 Y. Cho, Z. Sun, K. M. Lee, G. Zeng, S. Jeong, S. Yang, J. E. Lee, B. Lee, S.-H. Kang, Y. Li, L. Li, S. K. Kwak and C. Yang, *ACS Energy Lett.*, 2022, 96–106, DOI: 10.1021/acsenergylett.2c02140.
16 S. Jung, Y. Cho, Y. Ji, J. Oh, G. Park, W. Kim, S. Jeong, S. M. Lee, S. Chen, Y. Zhang and C. Yang, *Nano Energy*, 2022, 108059, DOI: 10.1016/j.nanoen.2022.108059.
17 Y. An, J. Oh, S. Chen, B. Lee, S. M. Lee, D. Han and C. Yang, *Polym. Chem.*, 2018, **9**, 593–602.
18 M. Jeong, J. Oh, Y. Cho, B. Lee, S. Jeong, S. M. Lee, S.-H. Kang and C. Yang, *Adv. Funct. Mater.*, 2021, **31**, 2102371.
19 M. Jeong, B. Lee, Y. Cho, J. Oh, S. M. Lee, J. Lee and C. Yang, *Small Methods*, 2020, **4**, 1900696.
20 Y. Cho, T. Kumari, S. Jeong, S. M. Lee, M. Jeong, B. Lee, J. Oh, Y. Zhang, B. Huang, L. Chen and C. Yang, *Nano Energy*, 2020, **75**, 104896.
21 H. Huang, X. Li, S. Chen, B. Qiu, J. Du, L. Meng, Z. Zhang, C. Yang and Y. Li, *J. Mater. Chem. A*, 2019, **7**, 27423–27431.
22 N. Yang, Y. Cheng, S. Kim, B. Huang, Z. Liu, J. Deng, J. Wang, C. Yang, F. Wu and L. Chen, *ChemSusChem*, 2022, **15**, e202200138.
23 Y. Xu, Y. Cui, H. Yao, T. Zhang, J. Zhang, L. Ma, J. Wang, Z. Wei and J. Hou, *Adv. Mater.*, 2021, **33**, 2101090.
24 N. K. Elumalai and A. Uddin, *Energy Environ. Sci.*, 2016, **9**, 391–410.
25 T. Jia, W. Zhou, Y. Chen, J. Han, L. Wang, F. Li and Y. Wang, *J. Mater. Chem. A*, 2015, **3**, 4547–4554.
26 Y. Terao, H. Sasabe and C. Adachi, *Appl. Phys. Lett.*, 2007, **90**, 103515.
27 A. K. K. Kyaw, D. H. Wang, V. Gupta, W. L. Leong, L. Ke, G. C. Bazan and A. J. Heeger, *ACS Nano*, 2013, **7**, 4569–4577.
28 S. Jung, Y. Cho, S.-H. Kang, S.-J. Yoon and C. Yang, *Sol. RRL*, 2022, **6**, 2100819.